Journal of Computer-Aided Molecular Design (2005) 19: 149–163
DOI 10.1007/s10822-005-3692-7

Molecular design of two sterol 14α-demethylase homology models and their interactions with the azole antifungals ketoconazole and bifonazole

Bernd Rupp[a], Stephan Raub[b], Christel Marian[b] & Hans-Dieter Höltje[a,*]
[a]*Institute of Pharmaceutical Chemistry, Heinrich-Heine-University Düsseldorf, Universitätsstrasse 1, 40225, Düsseldorf, Germany;* [b]*Institute of Theoretical and Computational Chemistry, Heinrich-Heine-University Düsseldorf, Universitätsstrasse 1, 40225, Düsseldorf, Germany*

Received 31 August 2004; accepted 14 March 2005

Key words: C. albicans CYP51, CYP51, heme-imidazole force-field parameters, homology models, human CYP51, sterol 14α-demethylase

Summary

Sterol 14α-demethylase (CYP51) is one of the known major targets for azole antifungals. Therapeutic side effects of these antifungals are based on interactions of the azoles with the human analogue enzyme. This study describes for the first time a comparison of a *human* CYP51 (HU-CYP51) homology model with a homology model of the fungal CYP51 of *Candida albicans* (CA-CYP51). Both models are constructed by using the crystal structure of *Mycobacterium tuberculosis MT-CYP51* (PDB code: 1EA1).The binding mode of the azole ketoconazole is investigated in molecular dynamics simulations with the GROMACS force field. The usage of special parameters for the iron azole complex binding is necessary to obtain the correct complex geometry in the active site of the enzyme models. Based on the dynamics simulations it is possible to explain the enantioselectivity of the human enzyme and also to predict the binding mode of the isomers of ketoconazole in the active site of the fungal model.

Introduction

Cytochrome P450 sterol demethylase (CYP51) catalyses the oxidative removal of the 14α-methyl group of lanosterol and 24-methylene-24,25-dihydrolanosterol in yeast and 24,25-dihydrolanosterol in mammals to give $\Delta^{14,15}$-desaturated intermediates in ergosterol (yeast) and cholesterol (mammals) biosynthesis. In the catalytic cycle, the substrate undergoes three monooxygenation reactions. In subsequent steps, the substrate first is converted to the 14-hydroxymethyl, then into a 14-carboxaldehyde, and in the last step into a 14-formyl derivative. Finally follows the elimination of the formyl group and the introduction of a 14,15 double bond in the sterol structure.

Azoles are known as a potent group of inhibitors of the fungal CYP51. Many different structures of this type of antifungals such as ketoconazole, bifonazole and fluconazole (see Figure 1) are used in therapy. The azole drugs are classified as imidazoles and triazoles [2]. They inhibit the CYP51 by a mechanism in which the heterocyclic nitrogen atom (N3 of imidazole and N4 of triazole) binds to the heme iron in the active site of the enzyme. Ergosterol depletion and an accumulation of precursor 14α-methylated sterols are the result of the inhibition of the enzyme. The decrease of the concentration of 14α-methylated sterols change the structure of the plasma membrane, making it more vulnerable to further damages and influence the activity of several

*To whom correspondence should be addressed. phone +49 211 8113661; Fax +49 211 8113661; E-mail: hoeltje@pharm.uni-duesseldorf.de

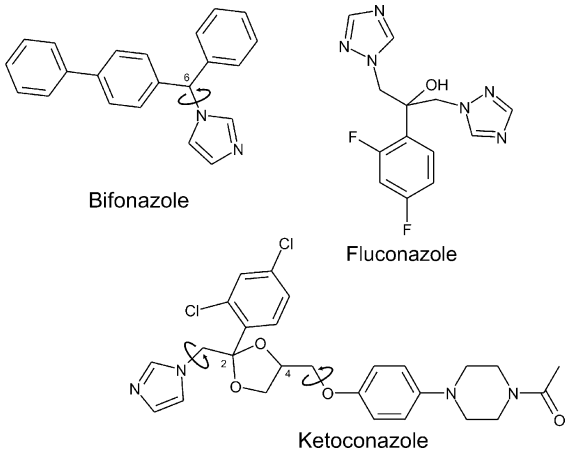

Figure 1. Structures of antifungals. Chiral centers and rotated dihedral angles are marked.

membrane-bound enzymes [3, 4]. A selective inhibition of this fungal cytochrome P450 enzyme reflecting the clinically important activity of azole antifungal agents is highly desired [5]. Up to now azole drugs are used in the treatment of deep-seated mycoses and life-threatening systemic infections. However, azole antifungal agents exhibit general toxicity because they are also able to coordinate with the heme iron in mammalian cytochromes [1]. For example, fatal hepatotoxicity by inhibition of the mammalian CYP3A4 and dramatic sterol lowering activity by inhibition of the mammalian CYP51 were reported [1]. Several extensive structure-activity studies have demonstrated the azole ring being the most important pharmacophoric feature for azole antifungals, but also toxicity is mainly attributed to the coordinative binding of the nitrogen atom of the azole to the heme iron [6]. This is one reason for the need to learn more about the characteristics of the active site of CYP51 of different species to design compounds with higher specificity for the fungal enzyme and to separate their activity from toxicity.

For an in-depth understanding of the diversity between CYP51 of *C. albicans* (CA-CYP51) and the *human* (HU-CYP51) enzyme molecular dynamics studies were performed based on homology models of the enzymes. The 3D structures of the models were constructed based on the crystal structure of the respective enzyme from *Mycobacterium tuberculosis* (MT-CYP51), which is documented in the PDB co-crystallized with fluconazole [7].

The pharmacophoric conformations of ketoconazole and bifonazole in the active site of both models were determined with the help of docking procedures in the enzymes and by fitting the enantiomers on the structure of fluconazole crystallized with MT-CYP51. These complex models were further investigated in molecular dynamics calculations employing the GROMACS force field [8]. In order to simulate the geometry and dynamic behaviour of the azole–heme complex correctly it was necessary to determine some lacking binding parameters describing the azole–heme iron interaction for the force field. To this end, quantum chemical *ab initio* calculations were performed on a model system described below. By application of these parameters in the molecular dynamics simulation it was possible to correctly describe the enantioselectivity of ketoconazole for the human enzyme and to estimate the enantioselectivity for the fungal enzyme.

Methods

Parameter calculation

Despite the enormous progress in the field of linear scaling quantum chemical methods, the CYP51 enzyme is too large for an *ab initio* treatment of its interaction with various ligands. For the computation of the interaction parameters, we therefore constructed a model system that is focused on the active site. The latter comprises an $Fe^{IV}L$ group (L is the substrate ligand) embedded in a protoporphyrin IX ring [9]. In CYP51, the sixth ligand is a cysteine of the protein backbone. In our model system the protoporphyrin IX ring was replaced by an unsubstituted porphyrin. This porphyrin–iron complex will be denoted by *FeP* in the following. It is well known [10] that the proximal ligand has a considerable effect on the iron–imidazole interaction. To test its influence on the present model system, two different thiolates were employed as fifth ligand: methylthiolate (CH_3S^-) and a complete cysteine residue (NH_2)$(COOH)CHCH_2S^-$.

The position of the imidazole ring (*Im*) relative to the active site of the enzyme can be described by means of three parameters (*cf.* Figure 2): The bond distance $d_{FeN^{Im}}$ between

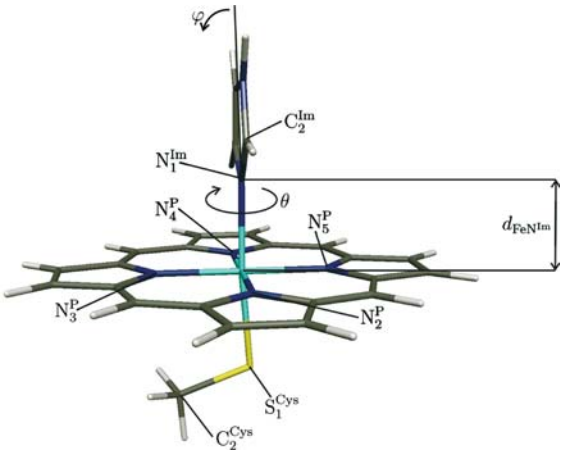

Figure 2. Model system (with MeS- as proximal ligand) and geometry parameters of the imidazole iron porphyrine interaction. The orientation of the ligand corresponds to a torsion angle $\theta^{(0)} = 0°$. A tilting angle $\varphi = 0°$ denotes a perpendicular position of the imidazole and prophyrine ring.

the iron atom and the N1 position of the imidazole, the torsion angle θ (dihedral angle $N_2^P - Fe_1 - N_1^{Im} - C_2^{Im}$), and the tilting angle φ.

Density functional theory (DFT) has proven to be a powerful tool for the investigation of transition metal compounds [11]. For our calculations we used density functional theory methods with the resolution-of-identity-approximation (RI-DFT) and Becke's exchange functional [12] with the correlation functional by Lee et al. [13] (denoted as BLYP) as implemented in the TURBOMOLE software suite [14, 15]. Every hydrogen atom was provided with a SV-P basis, all other atoms with a TZVP basis.

First, the geometry parameters of the model complexes were fully optimised. Constraint minimum energy paths were computed for fixed parameters $d_{FeN^{Im}}$, θ, and φ. To save computational expense, all CH- and NH-bonds were frozen to their equilibrium values in these calculations whereas all other degrees of freedom were relaxed. Coordinate driving was performed using the ef.x-tool [efx].

In Table 1, the geometric parameters of the fully optimised model systems are listed and compared with the data deduced from X-ray experiments of the crystal structure 1E9X. Estimated uncertainties in the crystal structure amount to approximately ± 0.001 nm for bond lengths and $\pm 3°$ for bond angles.

Table 1. Geometric parameters of the fully optimised model systems and the crystal structure.

	FeP-Im-Cys	FeP-Im-MeS	1E9X [1]
$d_{FeN}{}^{Im}$ nm	0.214	0.215	0.24
θ [°]	43.9	44.1	68.0
φ [°]	1.5	2.2	10.3
$d_{FeN_1^P}$ nm	0.203	0.202	0.202
$d_{FeN_2^P}$ nm	0.202	0.203	0.202
$d_{FeN_3^P}$ nm	0.202	0.202	0.204
$d_{FeN_4^P}$ nm	0.203	0.202	0.199
$d_{FeN}{}^{OutOfPlane}$ nm[a]	0.004	0.003	0.001
d_{FeS} nm	0.251	0.238	0.239

[a]The distance of the iron from the straight line between $N^P{}_2$ – $N^P{}_4$.

First of all, the computed geometry parameters appear to be rather insensitive to the particular type of proximal ligand. Comparing bond lengths determined for the model to those derived from the X-ray data, it strikes the eye that the distance between the central iron and the imidazole nitrogen in the crystal is appreciably larger than our theoretical values. On the other hand, we find an increased out-of-plane distortion of the iron atom in the model systems. For gaining a better insight, we have scanned the PDB for other complexes of a heme group with nitrogen-containing heterocycles. The results are displayed in Table 2.

In agreement with our theoretical findings, most of the structures reveal Fe–N distances between 0.21 and 0.22 nm. For the outlier, 1EA1, the reason could be steric repulsion of the 2,4-difluoro-benzene residue of fluconazole which comes close to the protoporhyrine. The somewhat larger tilt of the imidazole ligand in the crystal structure is probably due to steric effects. A histidine residue (H259) in the I-loop of the proteine backbone prevents a perpendicular position of the 4-phenyl-imidazole with respect to the porphyrine ring in the enzyme pocket.

The constrained minimum energy paths resulting from the Fe–N(Im) coordinate drives of the complex with the methylthiolate and cysteine proximal ligands are nearly perfect Morse potentials (Equation 1).

$$V_{\mathrm{Morse}}(d_{FeN^{Im}}) = D_{FeN^{Im}}[1-\exp(\beta_{FeN^{Im}}(d_{FeN^{Im}}-b_{FeN^{Im}}))]^2 \quad (1)$$

Table 2. Bond lengths of several Hem(Fe)–nitrogen bonds.

pdb name	Ligands	$d_{FeN^{Im}}$ nm	d_{FeS} nm	Resolution nm
1EA1	fluconazole, cysteine	0.234	0.231	0.221
1EGY	9-amino-phenantrene, cysteine	0.210	0.210	0.235
1F4T	4-phenyl imidazole, cysteine	0.213	0.264	0.193
1JIN	ketoconazole, cysteine	0.204	0.230	0.204
1MBI	imidazole, histidine	0.214	–[a]	0.200
1PHA	PFZ[b], cysteine	0.185	0.205	0.163
1PHD	4-phenyl imidazole, cysteine	0.228	0.232	0.160
1PHF	4-phenyl imidazole, cysteine	0.222	0.207	0.160
1PHG	metyrapone, cysteine	0.216	0.220	0.160

[a] $d_{FeN^{His}} = 0.204$ nm.
[b] PFZ = 1-(N-imidazolyl)-2-hydroxy-2-(2,3-dichlorophenyl)octane.

Fitting the parameters in expression (1) to the DFT curve yields a well depths of $D_{FeN^{Im}} = 54$ kJ mol^{-1}, an equilibrium distance of $b_{FeN^{Im}} = 0.213$ nm and a parameter $\beta_{FeN^{Im}} = 22.8$ nm^{-1}. Qualitatively, the same picture is obtained when the cysteine ligand is replaced by methylthiolate ($D_{FeN^{Im}} = 44$ kJ mol^{-1}, $b_{FeN^{Im}} = 0.215$ nm, $\beta_{FeN^{Im}} = 22.5$ nm^{-1}). Although this replacement had almost no effect on the complex geometry, we find a non negligible influence of the binding energy. In the latter case, the iron-sulfur bond is slightly stronger leading in turn to a weakening of the iron imidazole interaction ($\Delta E = 9.74$ kJ mol^{-1}).

In Figure 3a the constrained minimum energy path for a rotation about the Fe–N-bond (angle θ) of the FeP(Im)MeS complex with the length of this bond fixed to its optimized distance. The highest barrier ($\Delta E = 4.5$kJ mol^{-1}) can easily be overcome at temperatures in living cells. This mode can therefore be considered rather soft, i.e., distortions caused by the particular environment may be large. The energy profile along this coordinate was fitted to the periodic dihedral angle potential (Equation 2).

$$V(\theta) = k_\theta \cdot \left(1 + \cos\left(n \cdot \theta - \theta^{(0)}\right)\right) \qquad (2)$$

Although the cosine is just a simple dihedral potential and the minima in the calculated energy profile are not equal, the error appears to be rather small. Setting $n = 4$ we obtain a force constant $k_\theta = 1.86$ kJ mol^{-1} and a $\theta^{(0)} = 0°$.

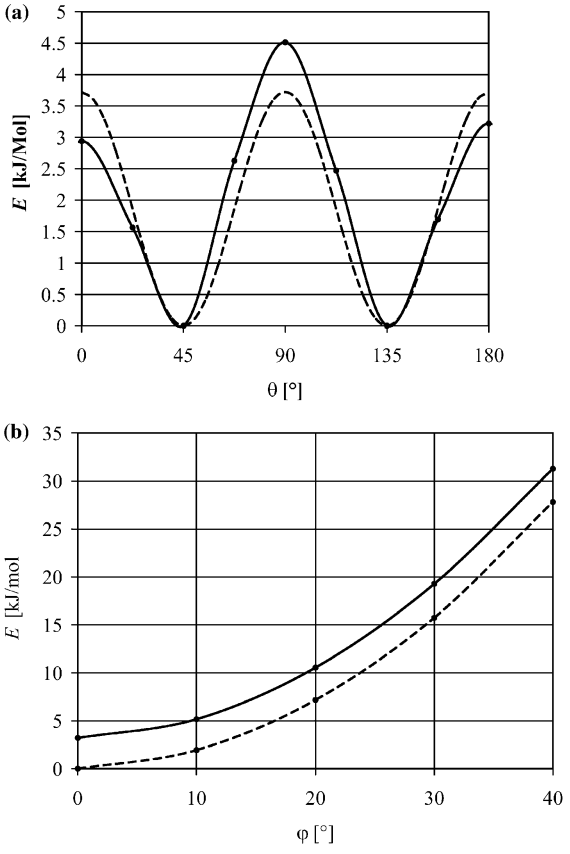

Figure 3. (a) Constrained minimum energy path for the torsion of the imidazole ligand in the FeP(Im)MeS complex. Solid line: DFT energy; dashed line: fitted cosine potential. For a definition of the torsion angle θ see Figure 2 and the text. (b) Constrained minimum energy path for a tilting of the imidazole ligand in the FeP(Im)MeS complex. Solid line: staggerd position ($\theta^{(0)} = 0°$); dashed line: eclipsed position ($\theta = 45°$). For a definition of the angles θ and φ see Figure 2.

Table 3. Sequence identities of the enzyme.

Seq. 1	Seq. 1	Global %	Active Site %
MT-CYP51	CA-CYP51	26.9	36.8
MT-CYP51	HU-CYP51	31.6	37.0
HU-CYP51	CA-CYP51	36.2	55.7
HU-CYP51	RAT-CYP51	93.4	97.5

Finally, the energy loss of the heme iron–azole nitrogen bond was determined by deflecting the azole ring. This deflection is a possible behaviour for the azole binding in the active site of a cytochrome P450 and a main reason for the differences in inhibitory activities of azoles. The energy expense for the torsion and deflection motions of the imidazole ligand appears to be nearly additive. This is seen from the two potentials displayed in Figure 3b. The upper curve was obtained for a torsion angle of $\theta^{(0)} = 0°$ (staggered position, maximum). It runs almost parallel to the curve obtained for the eclipsed orientation ($\theta = 45°$, minimum), which shows the independence of these two motions.

Construction of the enzyme models

As shown in Table 3 the sequence identity of the model sequences to the crystal structure is rather low because of the big differences in the sequence lengths. The largest diversity is found in the membrane anchor with 42 residues in *C. albicans* and 58 residues in the human sequence. In *C. albicans* a special 13 amino acids fungal loop (Figure 5 loop 8) has a negative effect on the overall identity of both sequences. The active site identity, however, is ~37% which is good enough for a reasonable alignment.

The alignments of the sequences of the crystal structure of MT-CYP51, the fungal enzyme of CA-CYP51 and the human CYP51 are shown in Figures 4 and 5.

The determination of the secondary structures was done using the secondary structure prediction program PSIPred [17]. Applicability of this program for cytochrome P450 enyzmes has been proven by the work of our group [18, 19]. Combining the results of the knowledge based alignment with the prediction of highly conserved

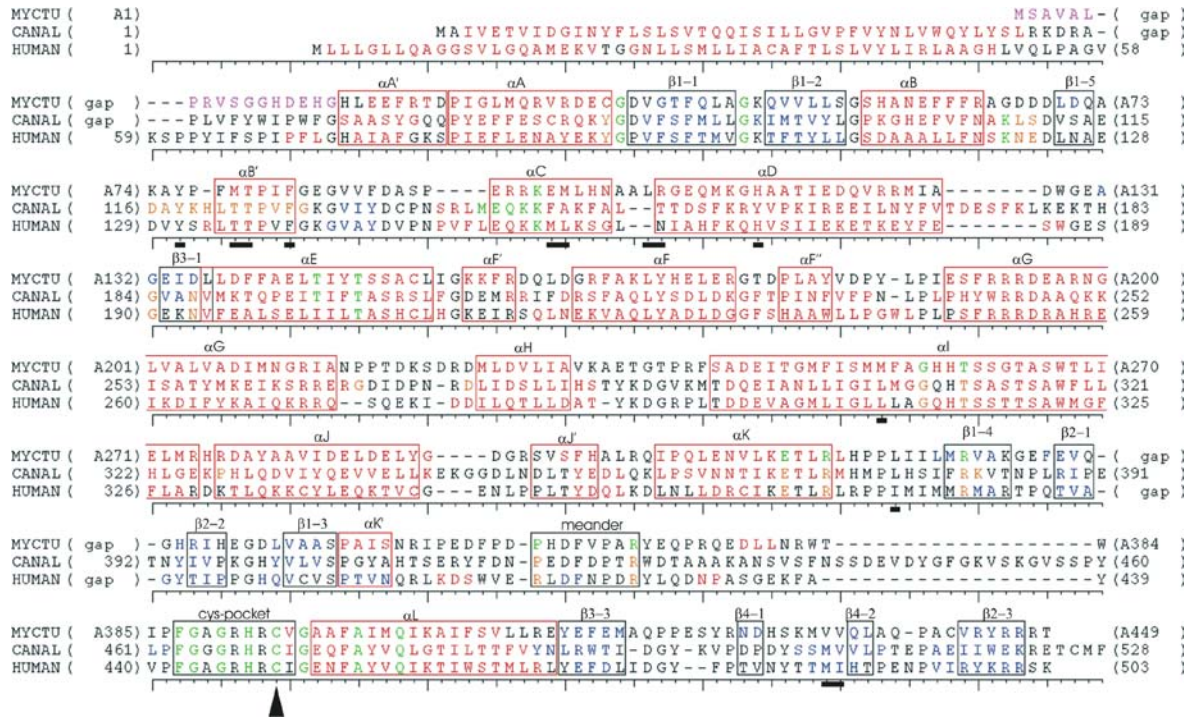

Figure 4. Alignment of the crystal structure sequence (MYCTU) with the sequences of *C.albicans* (CANAL) and of the human enzyme. Red boxes denote α helical regions and black boxes mark regions with β-sheet structures, the meander and the cys-pocket, respectively. Colour code of the sequences: Helices red, beta sheets blue, loops black, pin points green, and variable structures variable. Important binding residues are marked with a bar and the cysteine with a black triangle.

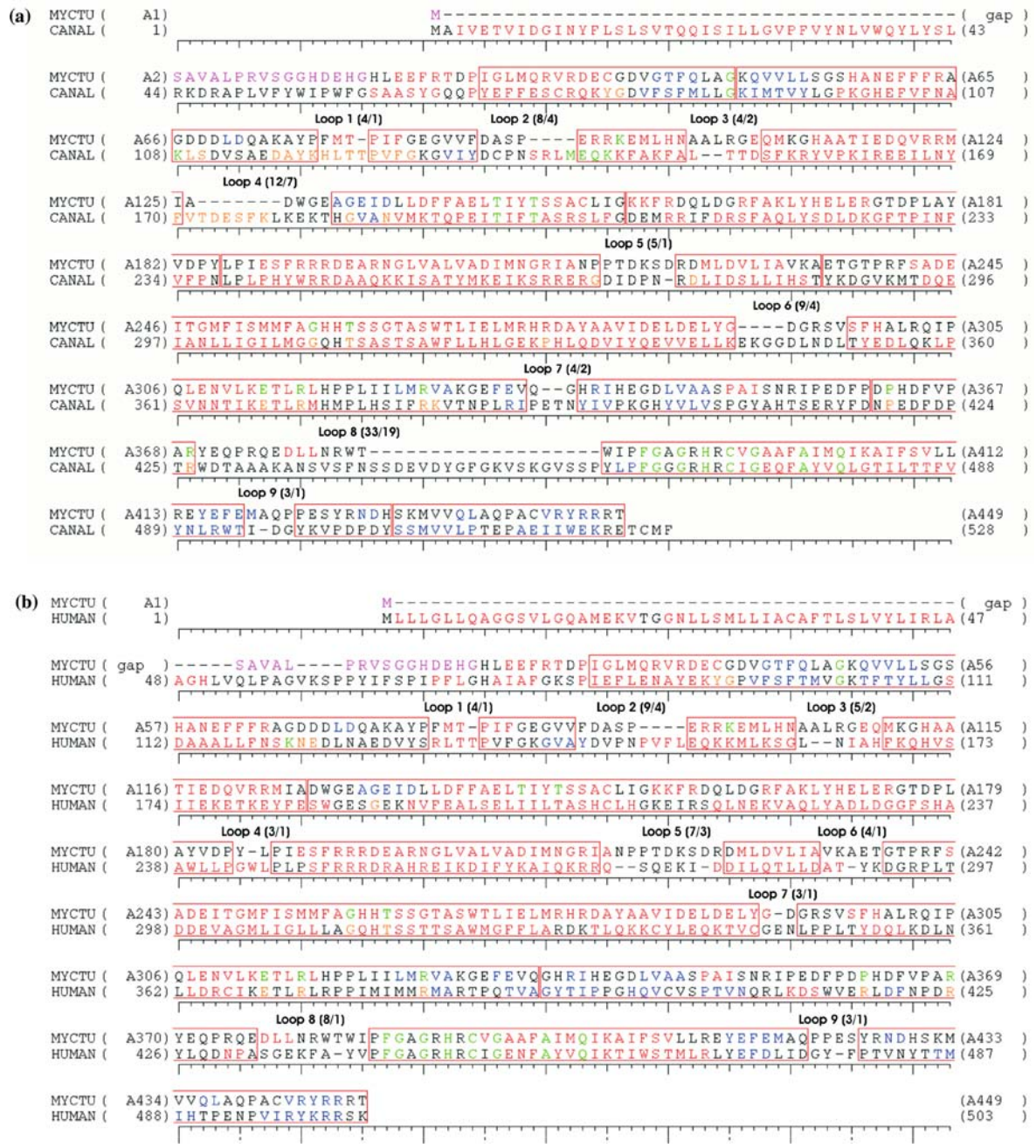

Figure 5. Alignment of the crystal- structure sequence (MYCTU) with the sequence of *C.albicans* (CANAL) (a) and the sequence of the human enzyme figure (b), respectively. Red boxes represent the regions of the crystal structure used for the construction of the model. Loop regions are marked by the word ''loop'' and the number of the structure. The first number in the brackets gives the length of the constructed loop, the second number is the length of insertion or deletion, respectively. Colour code: Helices red, beta sheets blue, loop black, pin points green and variable structures orange.

secondary structural elements a stable 3D model of the protein could be generated.

Sixty-eight amino acid in the CA-CYP51 model of the *N*-terminal were indicated as membrane anchor of CYP51 in the publication of Lamb et al. [20] and therefore were omitted in model construction. In the human model 81 residues of the *N*-terminal correspond with the

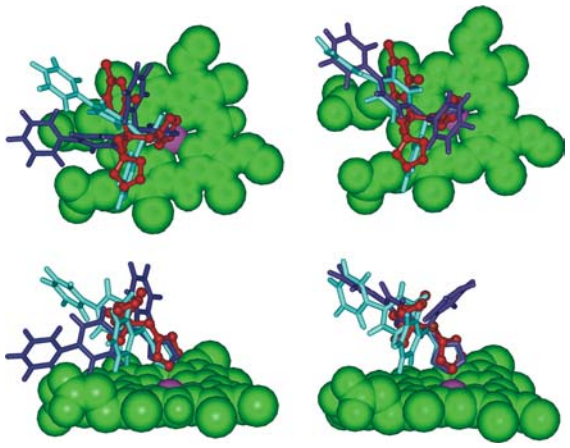

Figure 6. Docking of bifonazole in the active site of the C. albicans (left) and in the human enzyme model (right). Colour code: red = fluconazole (crystal structure), cyan = R-bifonazol, violet = S-bifonazol.

sequence of the membrane anchor of CA-CYP51 accordingly these residues were omitted in the human model.

MT-CYP51 was used as a template to assign the coordinates to the structurally conserved regions of both models. Some insertions had to be introduced to the model sequences because the lengths of the model sequences differ in 79 and 54 amino acids, respectively. All of these insertions are located in random coiled sequence segments at the surface of the enzymes. These were modelled using the loop search routine in the HOMOLOGY module of INSIGTH II [21].

After rough construction of the two models the splice points of different structural segments were adjusted by energy minimisation. During this procedure most parts of the structure were fixed, only the residues around the splice points could move freely. Next the models were superimposed to the template structure MT-CYP51 and the heme coordinates of CYP51 were copied to the model structures.

The protein geometry of the two models was refined by an intensive energy minimisation process using the GROMACS force field [8] with steepest descent and conjugate gradient algorithms. During minimisation the protein backbone of the conserved secondary structural elements was tethered with a force of 1000 kJ mol^{-1}.

Molecular dynamics simulations

For testing the stability of the enzyme models and determining the binding modes of ketoconazole and bifonazole isomers (see Figure 1) in the active site, several molecular dynamics simulations were performed (Figure 6).

The simulations of the model structures were performed under physiological conditions using the program GROMACS [8]. For this purpose, the protein was centred in a box containing 40 sodium and 40 chloride ions (equivalent to a 0.9% NaCl solution) and all simulations were carried out for a temperature of 310 K. Periodic boundary conditions were used to avoid surface artefacts at the box edges.

First step of every simulation was an intensive energy minimisation processed as shown in the section *construction of the enzyme models*.

The system was equilibrated over a period of 250 ps. During this time only the backbone of the conserved secondary structural elements was fixed. Subsequently a free simulation was performed for a period of 1000 or 1250 ps, respectively. During the course of the simulation the actual frame was stored every 5 ps.

Docking of the inhibitors

In order to allow for determination of the protein–ligand interactions, the stereoisomers of ketoconazole and bifonazole were docked into the active site of the two CYP51 models.

Two crystal structures, 1JIN and 1JIP [22], present a possible binding geometry in their active site for the 2R, 4S- and the 2S, 4R- isomer of ketoconazole. But there are several reasons why we could not use these binding modes directly for the docking in the active site of our CYP51 model. First, CYP eryf has a sequence identity smaller than 10% compared to the CYP51 sequence. Second, the secondary structure arrangement around the active site of the eryf is very different compared to cyp51 resulting in a significant change in the sterical features of this part. A third point is that the iron imidazole arrangement is skewed in the crystal structure, demonstrated by φ angles larger than 25° ($\theta \approx 45°$). Therefore the binding geometry of ketoconazole in the crystal structures is far from being ideal from the energetical point of view.

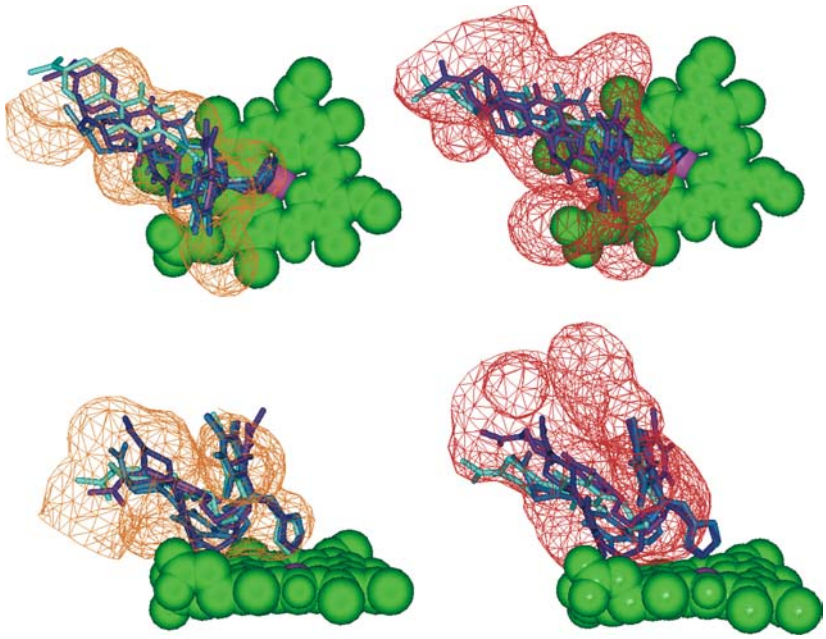

Figure 7. Docking of the ketoconazole isomers in the active sites of *C. albicans* (left) and the human enzyme model (right). The cavities of the active sites are shown in red or orange, respectively.

The structures of the ligands were taken from the Cambridge Structural Data base [23]. Isomers which were not available in the database were constructed by inverting the chiral centre. After the construction of the ligands the molecules were energy minimized.

In the first step of the dock routine, the imidazole ring of each of the drug molecules was superimposed to the triazole ring of fluconazole in the active site of the MT-CYP51 crystal structure.

The docking of the bifonazole enantiomers is based on the position of the fluconazole co-crystallized in the CYP51 structure. The bifonazole enantiomers were manually fitted onto the fluconazole structure so that the volumes of the molecules overlap as completely as possible.

Due to stereochemical reasons (larger size of the molecular structure) the docking of the ketoconazole isomers was more difficult. The strategy in this case was, starting from the imidazole coordinates, to fit the whole structure as good as possible into the cavity of the active sites of both models (see Figure 7). In order to find an acceptable conformation of ketoconazole in the cavity the dihedral angles (shown in Figure 1) were rotated in increments smaller than 15°. After the fit of the ligands subsequently a structure refinement of the ligands was performed by an intensive energy minimisation as shown in *construction of the enzyme models*.

Before starting the molecular dynamics simulations, the heme–imidazole bond was equipped with the parameters mentioned above. The dynamics simulations were performed as described in the section *molecular dynamic simulations*.

Results and discussion

Model stability

In order to allow for a better assessment of model stability a comparable dynamics simulation using the same parameters and conditions was performed for the MT-CYP51 crystal structure without fluconazole in the active site.

The dynamic behaviour and the structural changes of the proteins in the course of the simulation period were analysed and compared in detail. An often used parameter indicating the structural flexibility is the root mean square deviation (RMSD). The maximum RMSD values of the CYP51 models and the MT-CYP51 crystal structure calculated over all atoms amount to

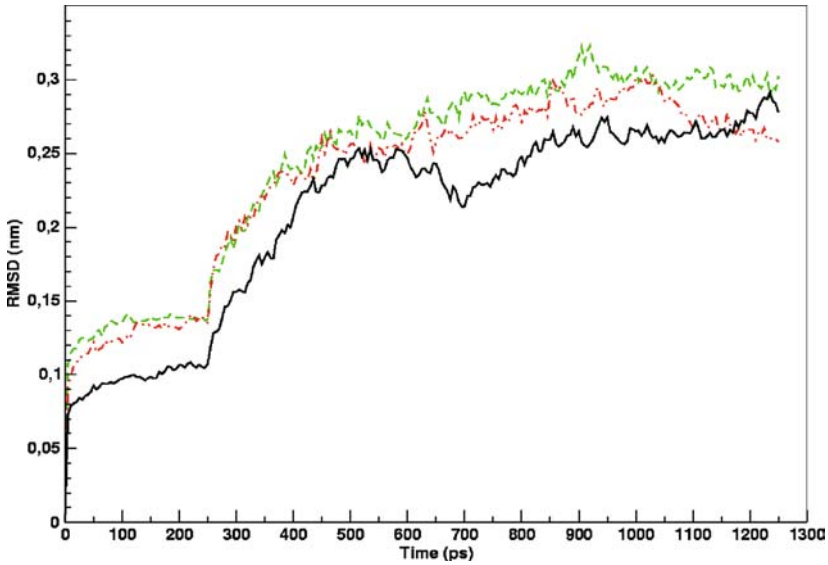

Figure 8. Curve gradient of the RMSD for molecular dynamics simulations of the crystal structure (black), of the C. albicans model (red (···)), as well as human enzyme model (green(- - -)).

0.28 nm (CA-CYP51), 0.31 nm (HU-CYP51) and 0.25 nm (MT-CYP51), respectively (Figure 8). Both models show slightly decreased stability as can be deduced from the RMSD values. The differences are so small, however, that the behaviour can be rated as comparable.

In order to analyse the source of the slightly decreased stability in more detail the RMS fluctuation (RMSF values) of every residue of all three protein structures were measured. As shown in Figure 9 only few residues exhibit larger RMSF values provoking protein flexibility. Nearly all of the flexible parts of the model proteins correspond to flexible structures of MT-CYP51 or to loop regions (see Figure 11).

Another interesting parameter for the assessment of protein quality is the ϕ/ψ-angle distribution (Ramachandran plot) of the protein structure

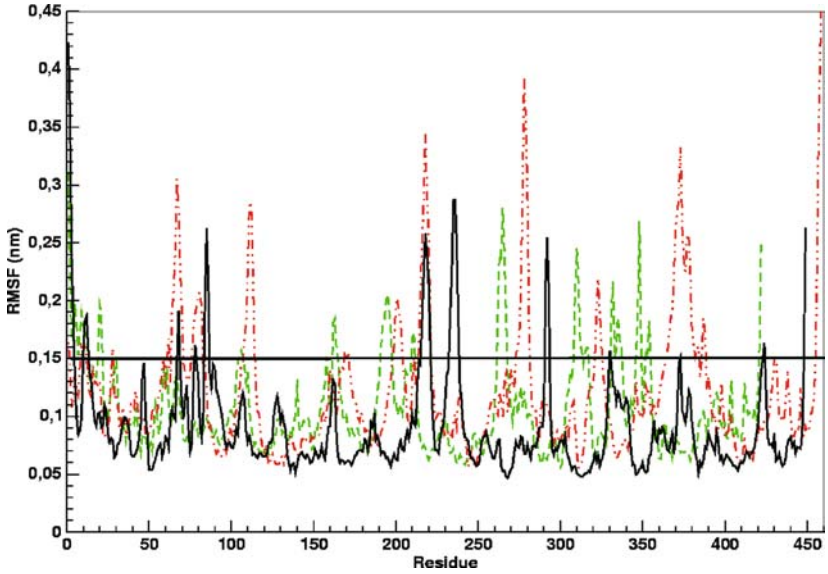

Figure 9. RMSF gradients for molecular dynamics simulations of the crystal structure (black), the model of *C. albicans* (red (···)), and the model of the human enzyme (green (- - -)).

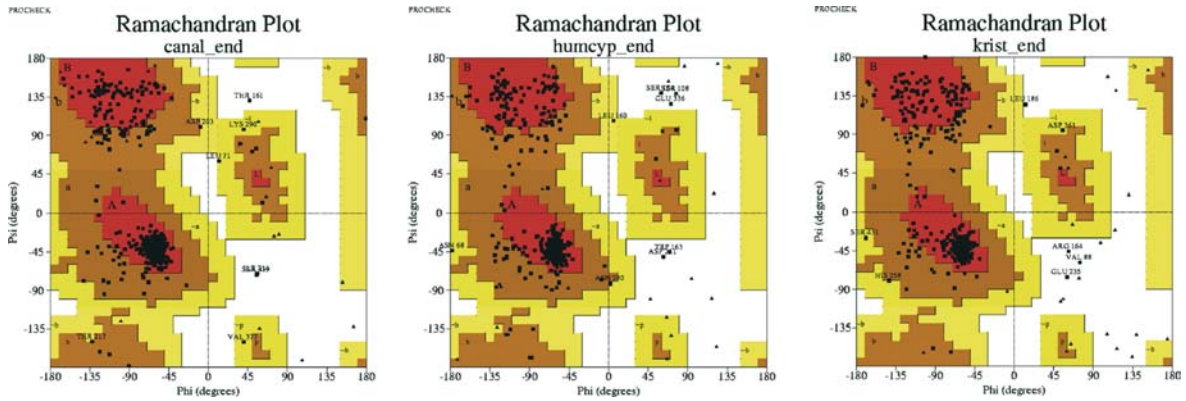

Figure 10. Ramachandran Plots for the last frames of the molecular dynamics simulations of the crystal structure (right), the model of *C. albicans* (left), and the model of the human enzyme (middle). The most favoured and the favoured regions are coloured red and brown, respectively. Yellow regions are the generally allowed, disallowed regions are white.

after the dynamics simulation. Showing more than 97% of the residues located in the two ''core'' (favoured and most favoured) regions (see Figure 10), the Ramachandran plots of all structures are of acceptable quality.

Only three residues in the human and five residues in the *C. albicans* model were found in the ''disallowed'' regions, but also three residues of the crystal structure were located in the ''disallowed'' regions. All these residues are found at the surface of the protein structure far away from the active site (Figure 11). These results demonstrate that the structures of both models have equivalent stability and good structural quality, when compared to the MT-CYP51 crystal structure.

Protein–Inhibitor interactions

The molecular dynamics simulations of the corresponding inhibitor–enzyme complexes for all four ketoconazole enantiomers as well as the two bifonazole isomers were carefully analysed. For

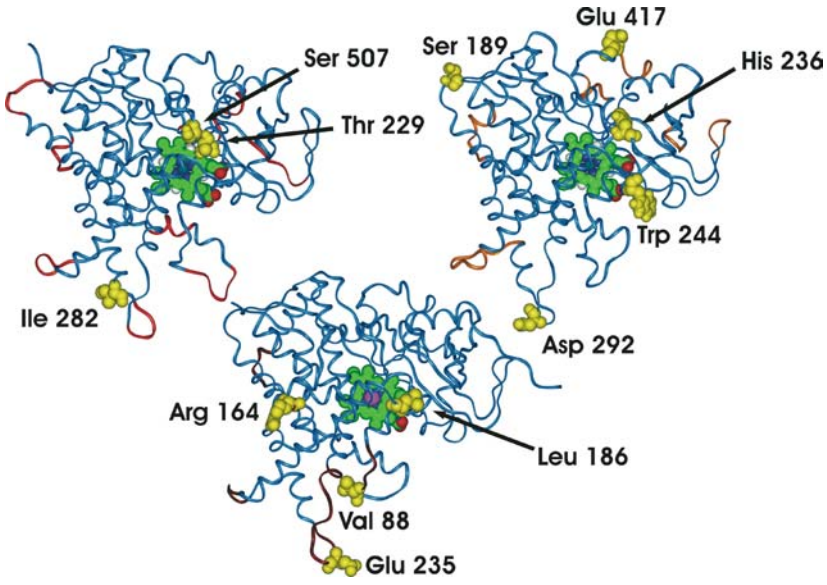

Figure 11. Structure of the last frame of the molecular dynamics simulations of the crystal structure (middle), the model of *C. albicans* (upper right), and the model of the human enzyme (upper left). The backbone of all structures is shown in blue. Flexible parts of the structures are displayed in dark red, red, and orange, respectively. Residues in disallowed regions of the Ramachandran plot are shown in yellow, the heme structure is atom type coded.

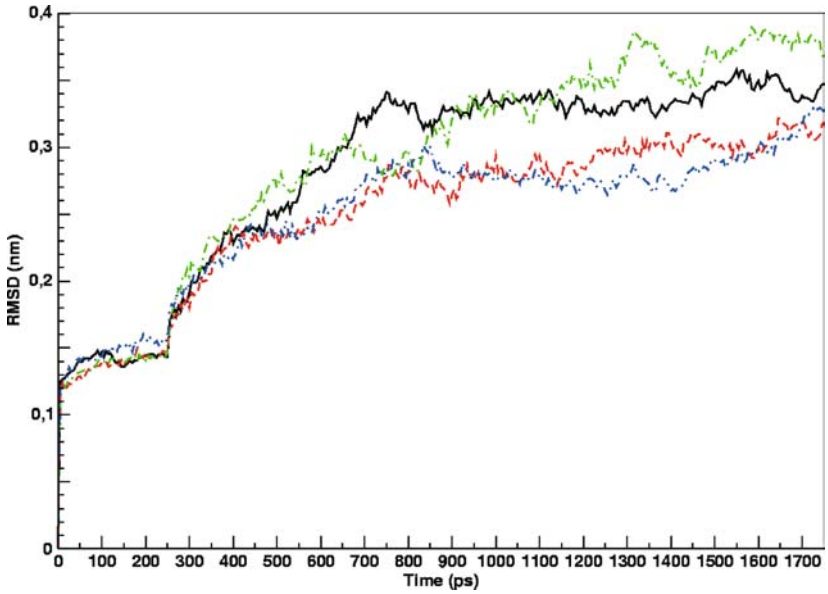

Figure 12. Curve gradient of the RMSD for molecule dynamics simulations of the ketoconazole isomer in the human enzyme. In black the 2R,4R- in red (- - -) the 2S,4R-, in green (·-) the 2S,4R and in blue (·- -) the 2S,4S-complexe simulation are shown.

this analysis, specific interactions were detected and their stabilities were evaluated.

In Figures 12 and 13 the behaviour of the protein in the complex with ketoconazole in the active site of the human enzyme is shown as example for the simulations performed with all ligands. The simulations of the other complexes were done in a similar way to the one shown. In comparison to the behaviour of the free protein (Figures 8 and 9) the RMSD increased slightly. The reason for the increased RMSD is a larger RMSF in three regions which are marked in Figure 13. The first region represents the BC-loop and B'-helix, the second the FG-loop and the third region is a central part of the I-helix. The increased flexibility in these regions of the protein is induced by the bound ligands. This observation is in good agreement with the B-factors determined for the crystal structure of MT-Cyp51 with bound fluconazole [7].

Next, the protein–inhibitor complexes were checked for H-bonds or other polar interactions. In the case of the ketoconazole complexes no additional polar interactions could be found between ligand and protein in the active site region besides the direct contact with the heme iron. However, close to the surface of the protein, the long polar substituent of ketoconazole is in contact with solvent molecules thereby building a partial solvent shell without any effect on the binding mode of the ligand.

Most of the specific contacts of the ligands are of lipophilic nature such as π–π interactions between aromatic groups of the inhibitors and the protein or aliphatic dispersive interactions. Because of the high sequence identity in the active sites of the *candida* and the human enzyme (see Table 3 and Figure 4) this type of binding was found to be almost identical in both isozymes. In Figures 14 and 15 the active sites of both models complexed with SR-ketoconazole isomers and bifonazole isomers are shown.

The last parameter analysed was the behaviour of the heme–iron nitrogen bond. The geometry of the heme ligand coordination was studied by measuring the deflection of the imidazole ring during the last 250 ps of the dynamics simulations. The measured angles are presented in Table 5 which show the averaged angle of imidazole ring deflection during the last 500 ps and 250 ps, respectively. Applying the results of the quantum chemical investigations the weakening of the ligand–enzyme interaction energies can be calculated based on measured deflections. The corresponding data are presented in Table 5 as energy loss given in kJ/mol.

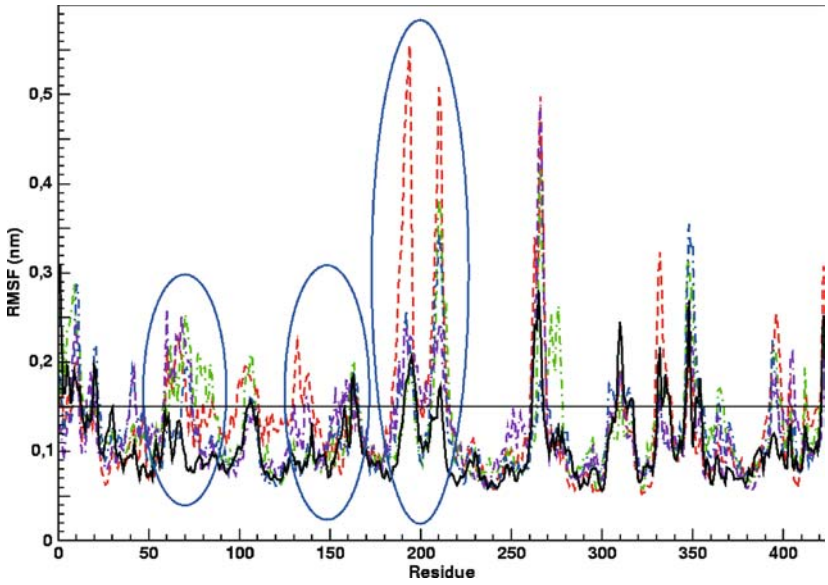

Figure 13. RNSF gradient for molecule dynamics simulations of the free human model (black) in comparison to the ketoconazole-complexes. Colour code: free human enzyme (black), complex with the 2R,4R- isomer red (—), with the 2R,4S-isomer green (·-), with the 2S,4R- isomer blue (··-) and with the 2S, 4S-isomer purple. The blue ovals mark flexible parts of the enzyme which were in contact with the ligand.

Binding of ketoconazole enantiomers

Table 5 shows the deflection angles of the imidazole ring for three ketoconazole isomers in the active site of the human enzyme model as well as the calculated decrease in interaction energy. The angles give clear evidence that the 2S, 4R-isomer exhibits the smallest variations from optimal binding geometry compared to the other isomers. Definitively the 2S, 4S-enantiomer shows the highest flexibility of this bond whereas the 2R,4S-enantiomer behaves slightly more rigid. The experimental data for the 2R, 4R-isomer unfortunately are of rather bad quality (more than 15% standard deviation) and therefore were omitted from the data set. In the following we will discuss the behaviour of the remaining three ketoconazole isomers in the MDS.

For deflection angles below 20° the energy of the coordinative bond is decreased by less than 20% when compared to the optimal bond geometry. At ring deflection degrees larger than 20° the energy loss increases dramatically because of the disruption of the iron–imidazole bond. These results correspond well with the biological data

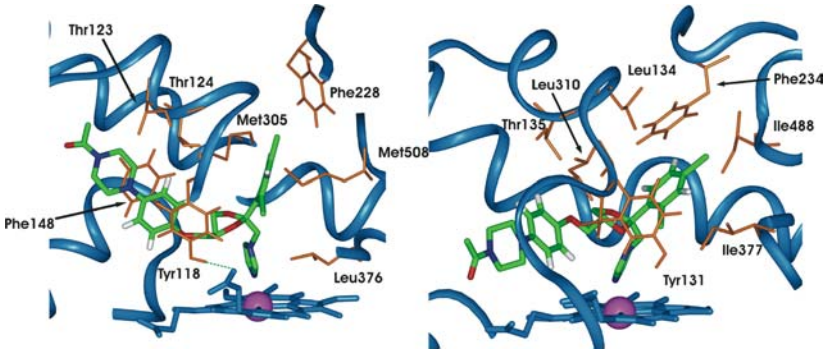

Figure 14. Complex structure of the 2S, 4R-isomer of ketoconazole in the active site the models of *C. albicans* (left), and the model of the human enzyme (right).The backbone and the heme are displayed in blue, important side chains in orange and the ketoconazole atom type coded.

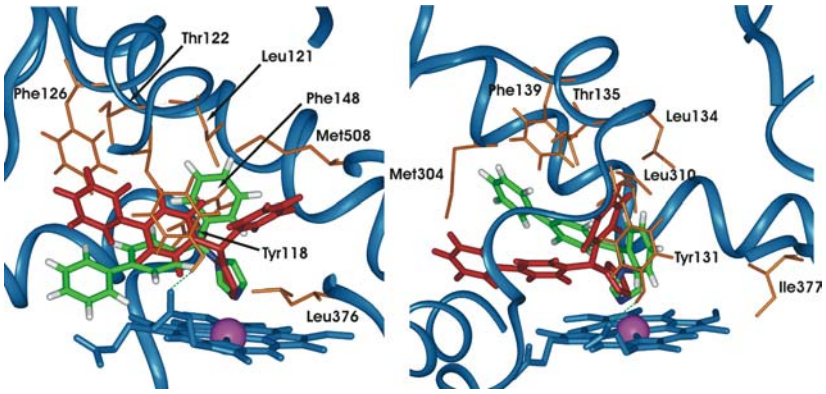

Figure 15. Complex structures of the bifonazole isomers in the active site the model of *C. albicans* (left), and the model of the human enzyme (right). The backbone and the heme are coloured blue, important side chains orange, the *R*-enantiomer is shown atom type coded and the *S*-enantiomer in red.

shown in Table 4 [24]. IC_{50}-values of ketoconazole in for rat liver CYP51 should be comparable to the human data, because of a sequence identity of 93.5% for the global sequence (see Table 3) [25] and as published in [7] (online suppl.) a 100% identical active site of both enzymes. By analysing the dynamics simulations, strong and weak inhibitors of the human enzyme can be identified very well if the differences in the IC_{50} values exceed a factor of 20. In case of inhibitors showing smaller IC_{50} differences, the dynamic behaviour of the complexes was found to become indistinguishably similar.

The analysis of the deflection of the imidazole ring of the ketoconazole enantiomers in the active site of *C. albicans* is also shown in Table 5.

Binding geometries of the four enantiomers of ketoconazole in the models of the human as well as the C.albicans enzymes differ most significantly in their behaviour towards the iron center of the heme system. As has been mentioned before the size of the deflection angle of the imidazole moiety of the inhibitor molecules is decisive for the interaction energies. In this respect the 2S, 4R-enantiomers shows a smaller degree of deflection in both enzyme models when compared with the other isomers. The 2R, 4S- and 2S, 4S-isomers show a similar more flexible intermediate behaviour. It was found, however, that the imidazole ring deflection for all enantiomers is significantly smaller in the *C. albicans* model than in the human enzyme model. The results coincide very favourably with experimentally derived inhibition constants which were published by Lamb et al. [26]. These studies identified an IC_{50} for the RS/SR racemate of 0.06 μM for the *C. albicans* and 0.5 μM for the human enzyme.

Table 4. IC_{50} Values of the ketoconazole isomers in the active centre of rat liver CYP51 [20].

IC_{50}-Values (μM)			
stereoisomers			
2S,4S	2R,4R	2S,4R	2R,4S
1.60 ± 0.08	1.37 ± 0.19	0.047 ± 0.003	0.119 ± 0.007

Table 5. Averaged deflection angle (K) of the imidazole ring (normalized to $\theta = 45°$) during the last 250 ps of the ketoconazole and the last 500 ps of the bifonazole MDS, respectively, for the human as well as for the *Candida albicans* enzyme. The respective energy loss is given in Kj mol^{-1} in brackets.

Ligand	HU-CYP51	CA-CYP52
Ketoconazole		
2S, 4S	23.5 (9.0)	13.0 (3.2)
2R, 4S	21.3 (7.9)	18.6 (6.0)
2S, 4R	17.9 (5.5)	10.3 (2.0)
Bifonazole		
R	11.3 (2.5)	18.9 (6.5)
S	17.7 (5.3)	17.4 (5.2)

Binding of bifonazole isomers

Experimental data also are available for the bifonazole binding of the *C.albicans* lanosterol

demethylase [27]. The MIC_{50} amounts to 2 μg/nl and it was determinated that both enantiomers are comparably strong inhibitors [28]. According to the molecular dynamics simulations reported here (see Table 5) both enantiomers indeed behave similar at least in the active site of the *C. albicans* model. In the human enzyme model a different performance can be observed. Here the *R*-enantiomer forms a much more stable imidazole–iron bond than the *S*-enantiomer. This effect is of potential importance for the therapy of fungal infections, since the amount of unwanted side effects possibly could be reduced if only the *S*-bifonazole is applied because this enantiomer is a good inhibitor of *C. albicans* but a weak blocker of the human isozyme.

Conclusion

This study was carried out to describe two homology models of the CYP51 *C. albicans* and the human enzyme. In these models, we docked bifonazole and ketoconazole to characterise the interactions of these inhibitors in the active site of the models. Our interest was to build representative models for later QSAR studies. The studies show that we were able to build the two models of the enzyme in comparable quality and stability when compared to the crystal structure of the CYP51. The two models presented here differ significantly from other models for the lanosterol demethylase reported earlier [29–35] because they are based on a high quality crystal structure and because different procedures for docking and molecular dynamics studies in aqueous environment have been used. The major aspect in our studies was to investigate the inhibitor binding and the complex behaviour. The calculations for the pure protein as well as the protein–inhibitor complex refinement were performed with molecular dynamics simulations in aqueous environment. With the analysis of the protein complex behaviour and the calculation of the deflection parameter it was possible to explain the biological data of different inhibitors.

The deflection of the imidazole ring which interacts with heme-iron was detected as the major descriptor for variation of the binding strengths of CYP51 inhibitors during these studies. Using the degree of the ring deflection as an structural interaction parameter it should be possible to perform QSAR studies for CYP51 inhibitors with potential predictive power.

References

1. Omura, T. and Ishimura, Y., Fujii-Kuriyama: Cytochrome-P450, 1993, ISBN: 3-527-30016-3.
2. Sheehan, D.J., Hitchcock, C.A. and Sibley, C.M., Clin. Microbiol. Rev., 12 (1999) 40.
3. Georgopapadakou, N.H. and Walsh, T.J., J. Antifungal Agents, 40 (1996) 279.
4. Lupetti, A., Danesi, R., Campa, M., Tacca, M.D. and Kelly, S., Trends Mol. Med., 8 (2002) 76.
5. Lamb, D.C., Kelly, D.E., Baldwin, B.C. and Kelly, S.L., Chem. Biol. Interact., 125 (2000) 165.
6. Fromtling, R.A., Clin. Microbiol. Rev., 1 (1988) 187.
7. Podust, L.M., Poulos, T.L. and Waterman, M.R., Proc. Nat. Acad. Sci., 98 (2001) 3068.
8. van der Spoel, D., van Buuren, A.R., Apol, E., Meulenhoff, P.J., Thieleman, D.P., Sijbers, A.L., Hess, B., Feenstra, K.A. and Berendsen, H.J., Gromacs User Manual version 3.0, 2001.
9. Sono, M., Roach, M.P., Coulter, E.D. and Dawson, J.H., Chem. Rev., 69 (1996) 2841.
10. Filatov, M., Harris, N. and Shaik, S., J. Chem. Soc., Perkin Trans., 2 (1999) 399.
11. Jonas, V. and Thiel, W., J. Chem. Phys., 102 (1995) 8474 (and references cited therein).
12. Becke, A.D., Phys. Rev. A, 38 (1988) 3098.
13. Lee, C., Yang, W. and Parr, R.G., Phys. Rev. B, 41 (1988) 785.
14. Ahlrichs, R., Baer, M., Häser, M., Horn, H. and Kölmel, C., Chem. Phys. Lett., 162(3) (1989) 165.
15. Treutler, O. and Ahlrichs, R., J. Chem. Phys., 102 (1995) 346.
16. Grimme, S., Gleichmann, M., Gastreich M. and Marian, C., ef.x, Universität Bonn.
17. The PsiPred Server at URL: http://bioinf.cs.ucl.ac.uk/psipred/.
18. Schappach, A. and Höltje, H.-D., Die Pharmazie, 56(6) (2001) 435.
19. Stahl, G., Höltje, H.-D., Die Pharmazie 60 (2005) 247.
20. Lamb, D.C., Kelly, D.E., Venkateswarul, K., Nigel, N.J., Frances, H., Bligh, J., Schunk, W.-H. and Kelly, S.L., Biochemistry, 38(27) (1999) 8733.
21. INSIGHT II, DISCOVER, HOMOLOGY, Biosym MSI (now accerlerys), 9685 Scranton Road San Diego, CA 9 2121–3752.
22. Cupp-Vickery, J.R., Garcia, C., Hofarce, A. and Mcgee-Estreada, K., J.Mol.Biol., 311 (2001) 101.
23. Cambridge Structural Database, Dr. Olga Kennard, F.R.S., Cambridge Crystallographic Data Centre, 12 Union Road, Cambridge CB2 1EZ, UK.
24. Rotstein, D.M., Kertesz, D.J., Walker, K.A.M. and Swinney, D.C., J. Med. Chem., 35(15) (1992) 2818.
25. Debeljak, N., Horvat, S., Vouk, K., Lee, M. and Rozmann, D., Arch. Biochem. Biophys., 379(1) (2000) 37.
26. Lamb, D.C., Kelly, D., Watermann, M.B., Stromsted, M., Rozman, D. and Kelly, S., Yeast, 15 (1999) 755.

27. Tafi, A., Costa, R., Botta, M., Santo, R.D., Corelli, F., Massa, S., Ciacci, A., Manetti, F. and Artico, M., J. Med. Chem., 45(13) (2002) 2720.
28. Botta, M., Corelli, F., Gasparrini, F., Messina, F. and Mugnaini, C., J. Org. Chem., 65(15) (2000) 4736.
29. Boscott, P.E. and Grant, G.H., J. Mol. Graph., 12 (1994) 185.
30. Höltje, H.-D. and Fattorusso, C., Pharm. Act. Helv., 72 (1998) 271.
31. Lewis, D.F.V., Wiseman, A. and Tarbit, M.H., J. Enzym. Inhib., 14 (1999) 175.
32. Ji, H., Zhang, W., Zhou, Y., Zhang, M., Zhu, J., Song, Y., Lü, J. and Zhu, J., J. Med. Chem., 43(13) (2000) 2493.
33. Rosselo, A., Bertini, S., Lappucci, A., Macchia, M., Martinelli, A., Rapposelli, S., Herreros, E. and Macchia, B., J. Med. Chem., 45(22) (2002) 4903.
34. Ji, H., Zhang, W., Zhang, M., Kudo, M., Aoyama, Y., Yoshido, Y., Sheng, C., Song, Y., Yang, S., Zhou, Y., Lü, J. and Zhu, J., J. Med. Chem., 46(4) (2003) 474.
35. Gollapudy, R., Ajmani, S. and Kulkarni, S.A., Bioorg. Med. Chem., 12 (2004) 2937.